

Study on Flow Fields in Centrifugal Compressor with Unpinched Vaneless Diffuser

TAMAKI Hideaki : Doctor of Engineering, P. E. Jp, Associate Fellow, Corporate Research and Development

The performance of centrifugal compressors strongly depends on their internal flow fields. Therefore, CFD (Computational Fluid Dynamics) is indispensable to the design of centrifugal compressors. CFD codes are usually validated by some representative data or compared with results calculated by other CFD codes, in order to ensure their accuracy. However, finding the estimation accuracy of any type of centrifugal compressor's performance requires continuously comparing experimental data obtained in the development of various centrifugal compressors with calculated results. This paper introduces one example of this by using a centrifugal compressor with an unpinched vaneless diffuser. In addition, flow behaviors in the inducer where CFD had qualitatively good agreement with experimental data were analyzed in detail.

1. Introduction

Turbochargers are effective for downsizing engines and enhancing their power, and help improve fuel efficiency by the reduction of friction loss in engines. Industrial compressors are used in various fields including the chemical industry, and fulfill roles in large air-conditioning equipment and as sources of pneumatic power in factories. Centrifugal compressors are often used as these compressors.

The performance of a centrifugal compressor strongly depends on its internal flow. CFD (Computational Fluid Dynamics) is one of the essential tools for obtaining information on such internal flows. In general, the accuracy of a CFD code is verified by a benchmark test against some representative experiment results or the calculation results of other CFD codes.^{(1), (2)}

On the other hand, designers of centrifugal compressors encounter opportunities to design compressors of various specifications. The accuracy of a CFD code depends on the specifications and shape of the compressor. It is impossible for designers to know the precision of the CFD code they are using for their design only from the results of verification of accuracy for limited specifications or shapes. Therefore, it is important to compare various measurement data obtained from the development process with the calculation results, determine the discrepancies resulting from the differences in their specifications or shapes, and make a database of that information.⁽³⁾⁻⁽⁵⁾ Continuously adding to this database allows them to enhance the accuracy of the design developed by using CFD (performance prediction) and shorten the development period of new compressors.

This paper describes a comparison between the results of experiments involving the combination of an unpinched vaneless diffuser and an impeller obtained from the development process of a centrifugal compressor for a marine-

use turbocharger and the calculation results using CFD. A centrifugal compressor is required to be highly efficient at a design point and have a wide operational range. In other words, it is essential to clarify the accuracy at an off-design point. The tested compressor in our experiment is intentionally designed to have a disturbed flow field from choke to surge. A high specific speed compressor with an unpinched vaneless diffuser was used. For such a compressor, the following flow fields can be expected.

- (1) Separated flows will occur near the shroud at the impeller outlet when the flow rate is near the choked flow.
- (2) Rotating stall tends to occur at the vaneless diffuser before occurrence of surge.

This paper reports the experiment results and compares them with the calculation results.

2. Experimental method

The major specifications of the compressor impeller used in our research are shown in **Table 1**. The rotational speed N is 55 400 min^{-1} , and the specific speed N_s is 0.15. N_s is calculated as $N/60 \times Q^{1/2}/Had^{3/4}$, where Q is the volumetric flow (m^3/s) and Had the adiabatic head (J/kg). **Figure 1** shows the tested compressor. The diffuser used is a vaneless diffuser (hereinafter VLD). A flow running out of the diffuser enters the axisymmetric collector. One static hole each was

Table 1 Impeller dimensions

Item	Unit	Specification
Impeller radius	mm	65.4
Inlet radius	mm	45.62
Outlet width	mm	10.2
No. of blades (full blades/splitter blades)	pcs	14 (7/7)
Outlet blade angle	degrees	-30

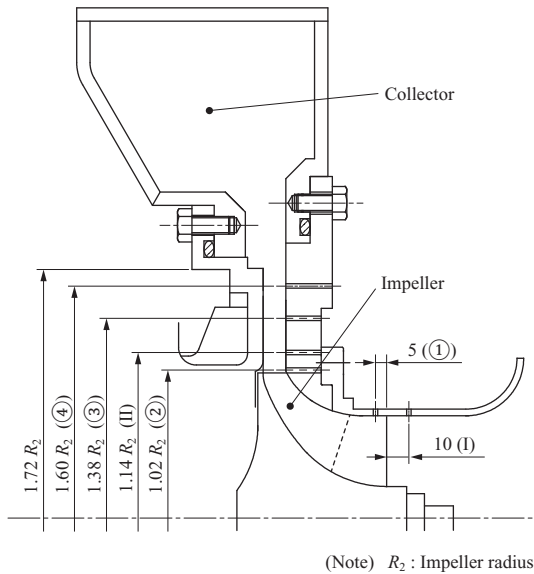


Fig. 1 Schematic of tested compressor (unit:mm)

provided at the impeller inlet (5 mm downstream from the tip of the full blade, hereinafter ①), the impeller outlet (1.02 R_2 ; R_2 is the impeller radius, hereinafter ②), the VLD (1.38 R_2 , hereinafter ③), and the diffuser outlet (1.60 R_2 , hereinafter ④). One high response pressure sensor was installed at each of ①, ②, and ③. Traverse measurement was conducted with a three-hole yaw-meter at a point 10 mm upstream of the leading edge of the full blade (hereinafter I) and a position 1.14 R_2 downstream of the impeller (hereinafter II). Furthermore, flows were visualized using the oil flow visualization method to observe the flow condition at the vaneless diffuser. An orifice was provided at the collector (compressor) outlet piping, and a choked condition was created in the orifice at small flow rates. Since the compressor can be stably operated when the flow rate is near the choked flow, it is therefore possible to make static measurement even in a flow rate area where the state of surge generally occurs. The contraction ratios of the orifice used in the research are 0.25 and 0.06.

3. Experiment results

3.1 Overall performance

Figure 2 shows the static pressure characteristics of the compressor at each position, which indicates the relationship between volumetric flow rate Q and the compressor outlet static pressure ratio. This figure also shows the static pressure ratio at ②, ③, and ④. The static pressure ratio in the figure is the ratio to the impeller inlet total pressure. Black points are the values obtained by installing the orifice at the collector outlet pipe. When $Q < 0.18 \text{ m}^3/\text{s}$, stable operation condition could not be generated unless an orifice was provided at the collector outlet. Therefore, the static pressure at the compressor outlet when $Q < 0.18 \text{ m}^3/\text{s}$ is not plotted in Fig. 2.

Figure 3 shows the pressure waveforms at ① and ③. The total width of the time axis (lateral axis) of the figure is 0.2 s at $0.37 \text{ m}^3/\text{s}$, 0.05 s at $0.28 \text{ m}^3/\text{s}$, and 0.1 s for other values,

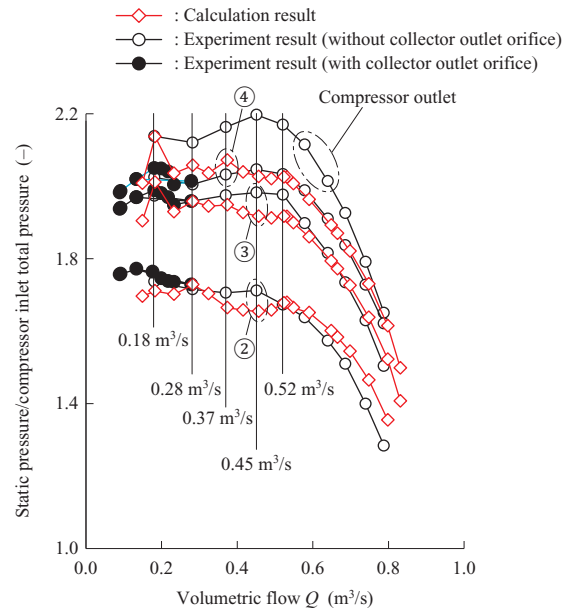


Fig. 2 Static pressure characteristics at each position of the compressor

while the vertical axis ΔP is static pressure (gage pressure: MPa). Periodic pressure changes are seen from $0.52 \text{ m}^3/\text{s}$ at the diffuser. For the inducer, no periodic pressure changes as clear as those at the diffuser are shown except at $0.37 \text{ m}^3/\text{s}$. This means there are unstable flows at the diffuser.

3.2 Impeller performance

Figure 4 shows part of the pressure waveforms at ①, the blade-to-blade static pressure distribution on the shroud side obtained from the periodically sampled and arithmetically averaged waveforms, and deviation σ of the static pressures between shroud side blades relative to the blade-to-blade static pressure P_0 in Fig. 4 indicates the total pressure at the inlet to the compressor, while vertical axis ΔP of $-(a)$ indicates static pressure (gage pressure). The periodicity of pressure changes breaks down, and the difference between the maximum and minimum of blade-to-blade static pressure reduces when $Q \leq 0.45 \text{ m}^3/\text{s}$. The deviation of blade-to-blade static pressure increases over the entire pitch. Based on these results, one may conclude that this flow rate is the inducer stall flow rate.

Figure 5 shows the distribution of axial velocity at position I. Y is the distance from the boss surface of the impeller, while H is the distance from the boss surface to the internal surface of the inlet pipe. $0.39 \text{ m}^3/\text{s}$ is the flow at which measurement of a backflow began at I. It is 13% smaller than the flow rate at which the periodicity breaks down, as just mentioned. Figure 6 shows the total temperature measured with two thermocouples (Temp-1 and Temp-2) installed before the bell-mouth. While the total temperature is kept almost constant until $0.28 \text{ m}^3/\text{s}$, when the flow rate is lowered to $0.21 \text{ m}^3/\text{s}$, it rapidly increases. This is because the flow that came to have a high temperature as a result of air compressed by the impeller flowed back and reached the upstream of the bell-mouth.

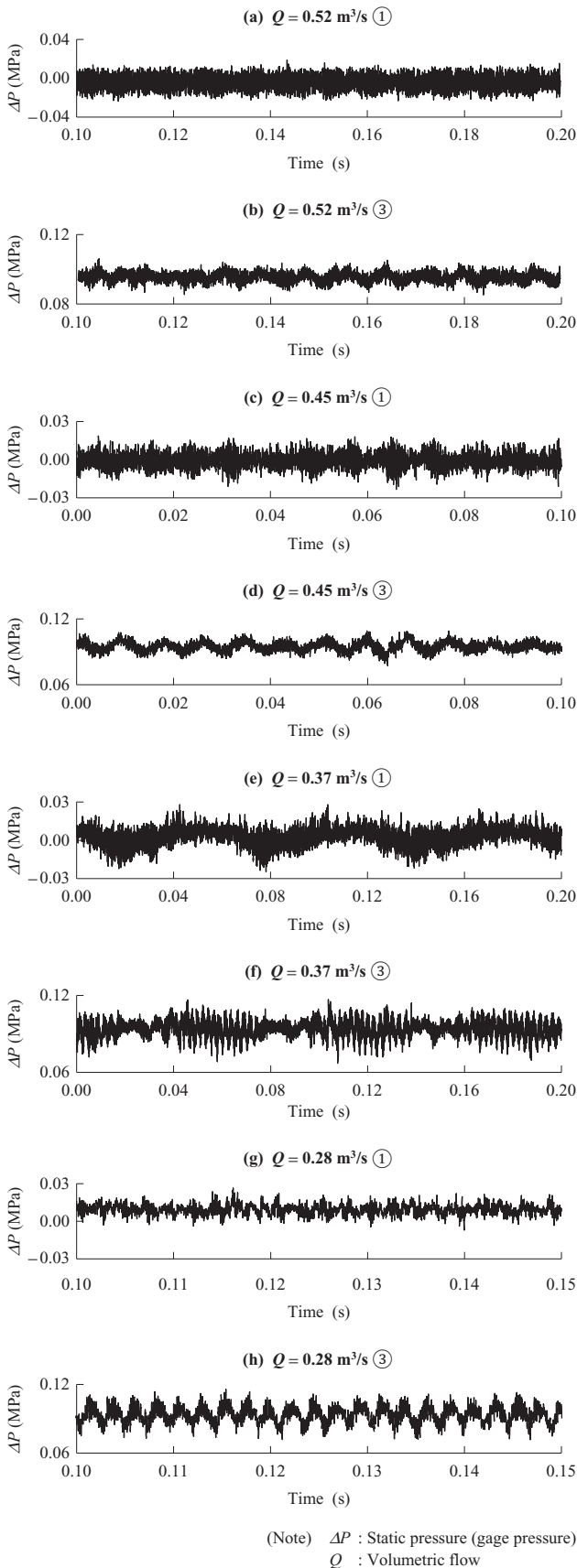


Fig. 3 Pressure fluctuation at ① and ③

3.3 Diffuser performance

Figure 7 shows the static pressure ratio between ② and ③. The maximum value of the static pressure ratio is at $0.52 \text{ m}^3/\text{s}$. It is therefore presumed that large changes occur in the flow field near this flow rate. Figure 8 shows the flow angles at position II and the total pressure distributions. Y_H is the distance from the hub surface, H_D is the diffuser width, $Y_H/H_D = 0$ is the hub, and $Y_H/H_D = 1$ is the shroud surface. Flow angles are the values measured from the radial direction (the area of the flow angle larger than 90 degrees corresponds to the backflow area). It can be seen that the backflow area exists in the area near the choke point on the shroud side. This backflow area shrinks with a reduction in the flow rate.

Flows that occurred in this experiment are visualized with the oil flow visualization method as shown in Fig. 9.

(1) When $Q = 0.67 \text{ m}^3/\text{s}$

(a) Hub side

The oil flow traces go from inside to outside in the same direction as the rotational direction of the impeller. No separation is observed.

(b) Shroud side

The oil flow traces move from inside to outside, which is opposite the direction of the impeller rotation. It indicates the flow is being separated from the VLD inlet.

(2) When $Q = 0.51 \text{ m}^3/\text{s}$

(a) Hub side

The oil flow traces move in the same direction as the impeller rotation from the VLD inlet to a certain radius position. More downstream from there, the pattern opposite the impeller rotation is observed. This suggests that backflows occur near the hub surface.

(b) Shroud side

The oil flow traces move in the direction opposite the impeller rotation at the VLD inlet side, not like the hub side. It is presumed that in this area backflows occur near the shroud. On the other hand, the pattern moving in the same direction as the impeller rotation is observed on the outlet side, and the separation that was observed at $0.67 \text{ m}^3/\text{s}$ has disappeared.

(3) When $Q \leq 0.38 \text{ m}^3/\text{s}$

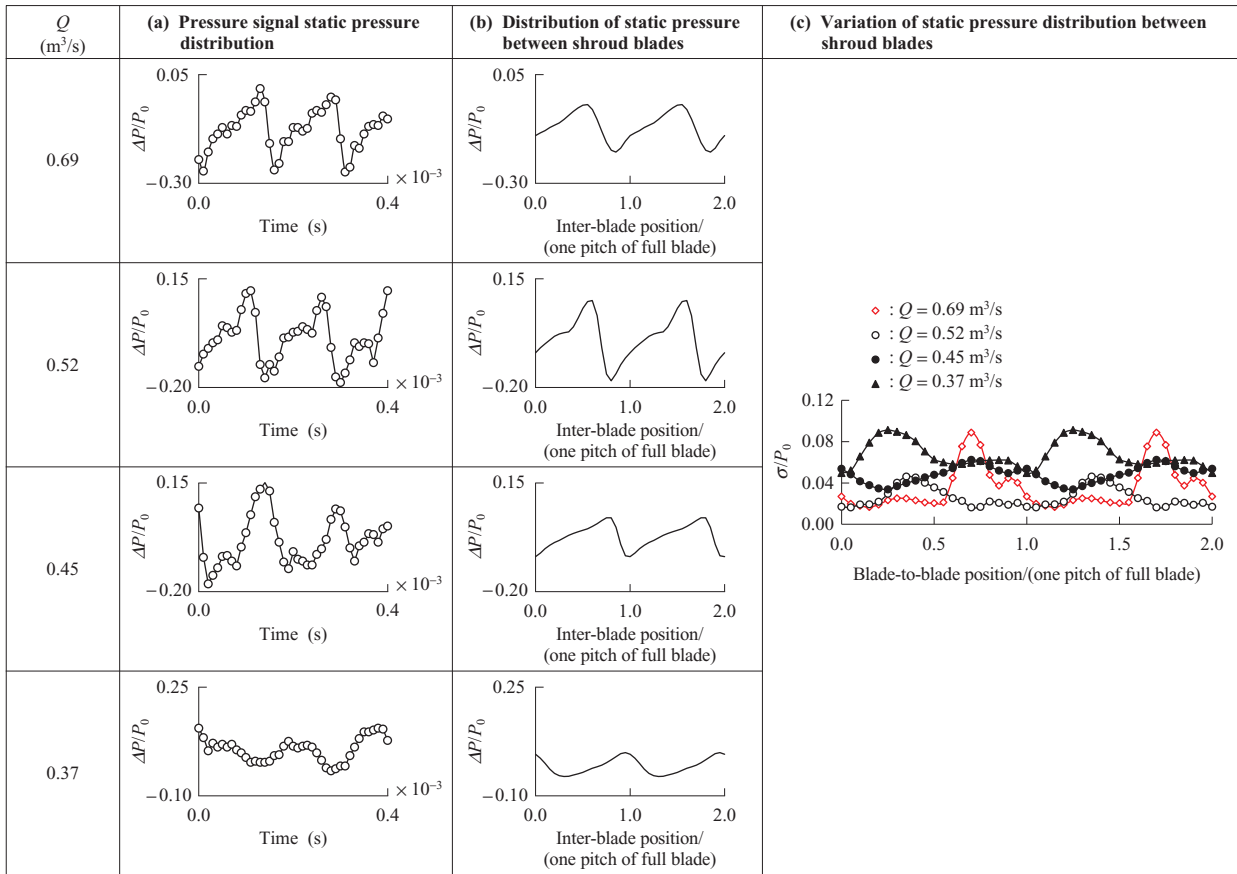
(a) Hub side

The oil flow traces are in the direction opposite the impeller rotation from the VLD inlet to the outlet. This shows that separation occurs from the VLD inlet to the hub side.

(b) Shroud side

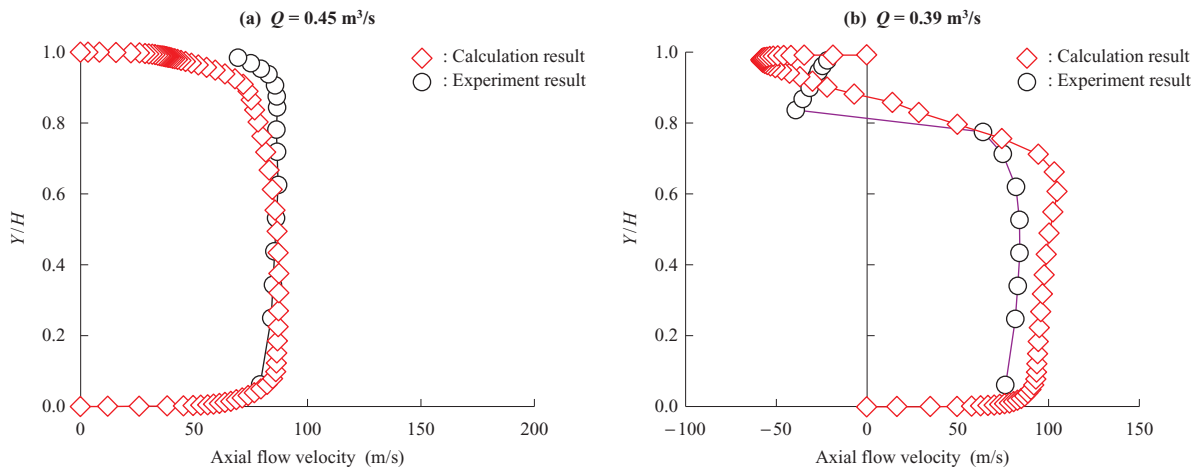
The oil flow traces move in the direction opposite the impeller rotation as in the case of the hub side, which indicates separation has occurred.

Figure 10 shows the waveforms of output pressure from the high-response pressure sensor at positions ② and ③. At ③, two high-response pressure sensors were installed at an interval of 60 degrees in the circumferential direction. At ③, a certain phase difference exists between two waveforms (see



(Note) P_0 : Compressor inlet total pressure
 ΔP : Static pressure (gage pressure)
 σ : Deviation of inter-blade static pressure
 Q : Volumetric flow

Fig. 4 Static pressure variation near shroud in between blades at ①



(Note) Q : Volumetric flow
 Y : Distance from impeller boss
 H : Distance from boss surface to internal surface of inlet piping

Fig. 5 Axial velocity distribution at I

the yellow solid lines in the figure), which suggests the occurrence of rotating stall.

3.4 Summary of the experiment results

The behavior of internal flows in the tested compressor is summarized along with the decrease in flows as follows:

- (1) Although the meridian plane curvature radius of the tested impeller is small, no pinch is provided at the VLD inlet. Therefore, flows occur with an area of separated flows (backflows) from near the choke point at the shroud side of the VLD.

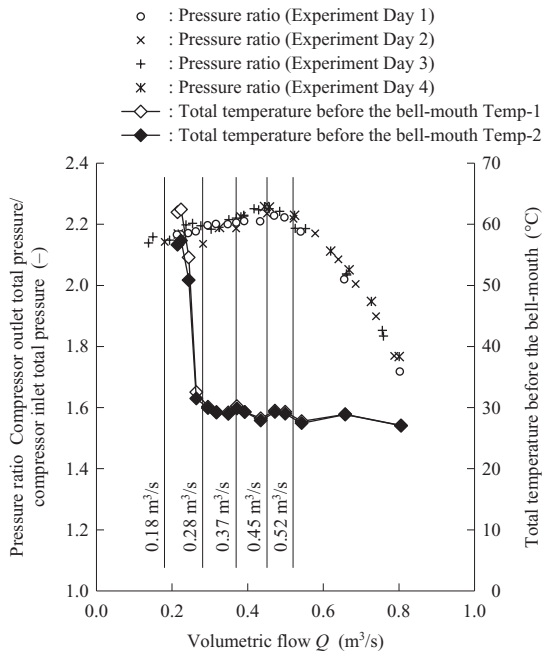


Fig. 6 Ratio of total-to-total pressure and total temperature just before bell-mouth

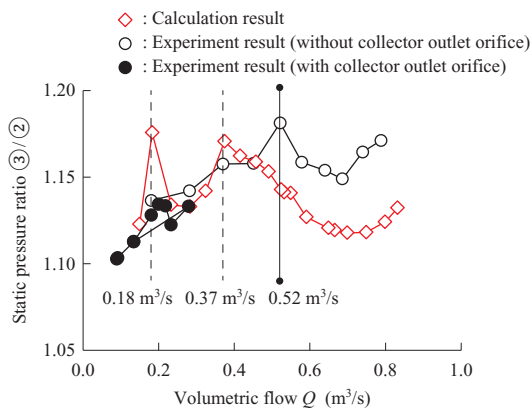


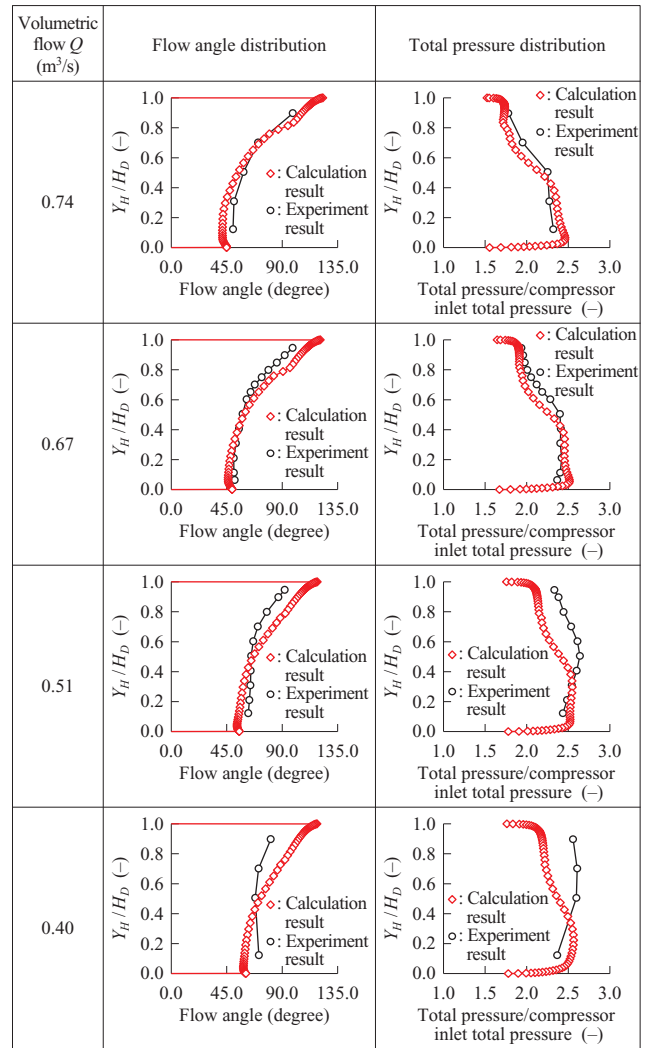
Fig. 7 Static pressure ratio between ② and ③

- (2) Separation occurs on the VLD hub side at 0.51 m³/s. Time-averaged measurement with a three-hole yawmeter did not confirm any separation on the hub side. However, since periodic pressure changes were observed, it indicates the occurrence of rotating stall. Therefore, it is presumed that flows are not steady and have non-axisymmetry. The occurrence of rotating stall at the vaneless diffuser of the tested compressor has been confirmed by PIV measurement⁽⁶⁾ in a different study as well.
- (3) The inducer stalls at 0.45 m³/s. The backflow area reaches the compressor inlet piping (I) at 0.39 m³/s and the bell-mouth inlet at 0.21 m³/s.
- (4) The flow rate just before surge is 0.18 m³/s.

4. Calculation results

4.1 Numerical calculation

Calculation was conducted with in-house CFD code developed by IHI.⁽⁷⁾⁻⁽⁹⁾ Chakravarthy-Osher's TVD scheme was used for



(Note) Y_H : Distance from hub surface
 H_D : Diffuser width

Fig. 8 Flow angle and total pressure distribution at II

the convective term, while the Spalart-Allmaras model was used for the turbulent flow model.

The computational grid used in the calculation is shown in **Fig. 11**. There are about 3 610 000 grids. Assuming that the flow is constant after it passes through the bell-mouth, a straight pipe parallel with the rotational axis is assumed for the inlet without considering the bell-mouth. A cavity is provided after 1.72 R_2 , downstream of the VLD, to simulate the experiment equipment. The hub surface is reduced in area to avoid the divergence of the calculation due to the occurrence of backflows at the outlet boundary. Although the collector is not considered, it is confirmed from the experiment that the static pressure is uniform in the circumferential direction at position ④. The steady calculation of the flow path for a single pitch of the impeller was conducted by applying the periodic boundary.

4.2 Overall performance

The static pressure at ②, ③, and ④ obtained from the calculations is shown in **Fig. 2**. The calculation results show good agreement with the experiment results at $Q \geq 0.52$ m³/s.

No.	Volumetric flow Q (m ³ /s)	(a) Hub side	(b) Shroud side
(1)	0.67		
(2)	0.51		
(3)	0.38		
(4)	0.20		

(Note) : Impeller rotation direction
 : Direction of oil flow traces from inner radius to outer radius

Fig. 9 Oil flow visualization (hub side (a) and shroud side (b))

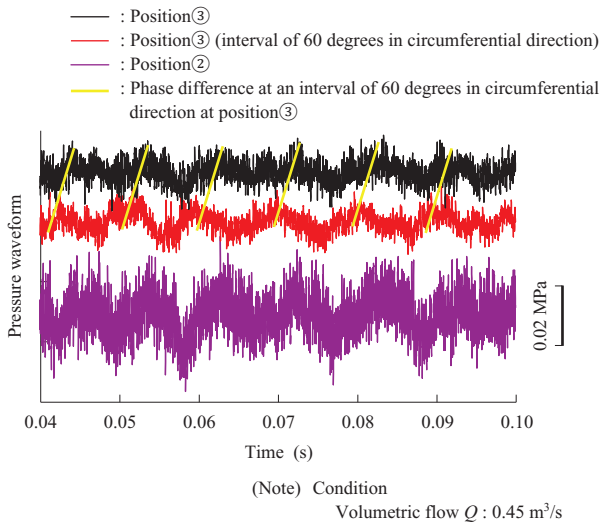


Fig. 10 Pressure variation at ② and ③

The flow rate at which the pressure characteristic curve takes a maximum value is 0.45 m³/s in the experiment and 0.52 m³/s in the calculation. The maximum value at ④ is 0.37 m³/s according to the calculation, while it is (0.28 to 0.32 m³/s) < Q < 0.52 m³/s at ② and ③. The calculation results show smaller values than the experiment values.

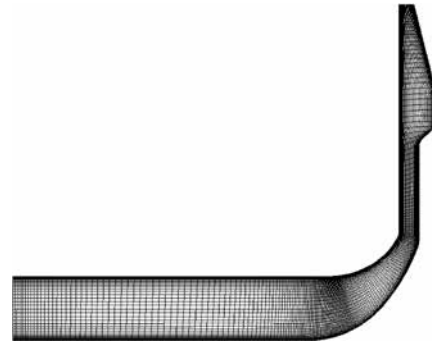


Fig. 11 Computational grid

Figure 7 shows the ratio of static pressure between ② and ③ obtained by calculation. While the trend is almost the same, the maximum value of the calculation results is shifted toward the smaller flow rate side than the experiment results. These results indicate that it is difficult for the calculation method used here to determine the steady (time-averaged) performance of the centrifugal compressor that accompanies rotating stall.

4.3 Flow patterns

4.3.1 Impeller

Figure 12 shows the calculation results of the distributions in the span direction of the flow angles and axial direction velocity obtained for ① by calculation, where Y is the distance from the hub surface and H_C is the distance from the casing to the hub surface. Y/H_C in the figure, which is ≥ 0.985 , is the clearance from the full blade to the casing (tip clearance). A backflow area occurred on the casing side between 0.43 and 0.45 m³/s. It almost matches the stall flow of the inducer estimated from Fig. 4. The distribution of the flow angles and the velocity in the axial direction at I, obtained by calculation, is shown in Fig. 5. The area where backflows occurred almost agrees with that of the measurement results. Qualitatively good agreement is shown between the experiment and calculation results. The flows at the inducer part were then examined in detail based on the calculation results.

Figures 13 to 15 show visualizations of the flow fields obtained by calculation. Figure 13-(a) and -(b) show the streamline that passes through near the suction surface at the leading edge of the full blade of the impeller and the streamline that passes through in the tip clearance, respectively. The figure shows the streamlines for two pitches of the full blade, and the limited streamlines are depicted on the front blade surfaces. The color of the streamlines indicates positive or negative of the velocity components in the axial direction. Red indicates “positive” (flow moving from the impeller inlet to the outlet), while blue indicates “negative” (flow moving from the impeller outlet to the inlet). Figure 13-(c) is the distribution of axial flow velocity in the tip clearance. As in the case of Figs. 13-(a) and -(b), red represents the zone where the axial flow velocity component is positive, while blue represents the negative zone. Since a tip leakage flow enters the clearance between the adjacent blades almost perpendicularly to the suction

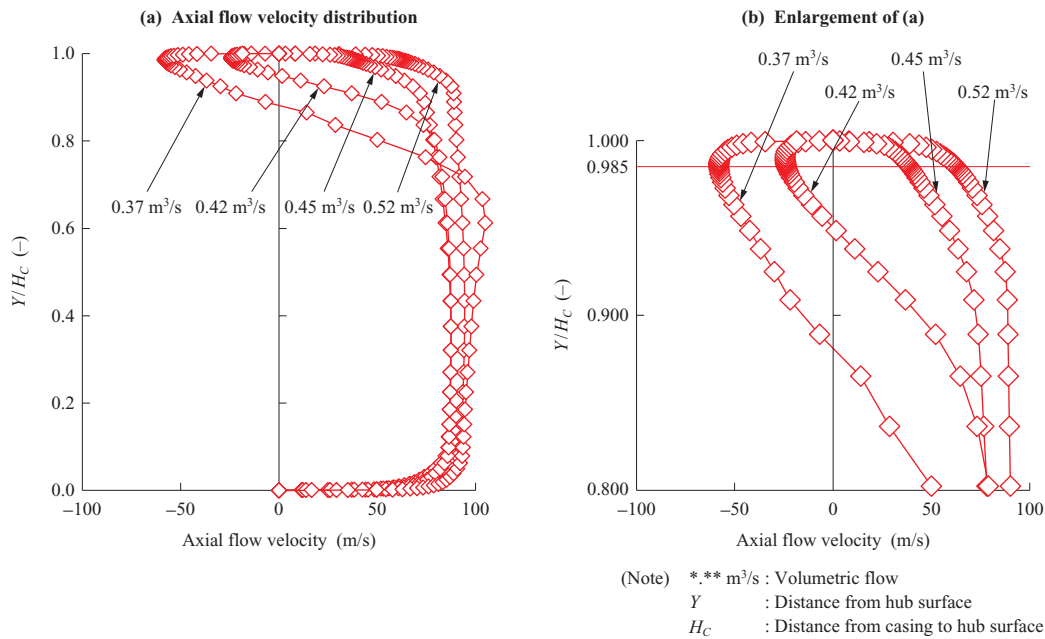


Fig. 12 Calculated axial velocity distribution at ①

surface, it has a negative axial flow velocity. This tip leakage flow joins the main flow that has a positive axial flow velocity and moves downstream with the main flow (Fig. 13-(d)). Therefore, we can estimate the zone of the tip leakage flow and the boundary plane between the main flow and the tip leakage flow from Fig. 13-(c).⁽¹⁰⁾ These figures allow us to infer the condition of the flow field at each flow rate (flow pattern) as follows:

- (1) When $Q = 0.70 \text{ m}^3/\text{s}$

Separation bubbles (two-dimensional separation) occur at the leading edge of the suction surface of the full blade. The tip leakage flow forms a tip leakage vortex and joins the main flow in the impeller.

- (2) When $Q = 0.52 \text{ m}^3/\text{s}$

Leading edge separation reaches the blade tip and is released to the main flow as separation bubbles (three-dimensional separation). The most upstream part of the main flow and the tip leakage flow (boundary plane) forms the tip leakage vortex and approaches the leading edge of the adjacent full blade (impeller inlet surface).

- (3) When $Q = 0.49 \text{ m}^3/\text{s}$

The boundary plane between the main flow and the tip leakage flow arrives at the upstream point of the impeller inlet plane. The flow pattern is almost the same as that at $0.52 \text{ m}^3/\text{s}$.

- (4) When $Q = 0.45 \text{ m}^3/\text{s}$

The boundary plane between the main flow and the tip leakage flow arrives at the point upstream of the impeller inlet plane and re-enters the impeller. Since a backflow area exists near the casing on the impeller inlet surface, the blockage caused by this backflow accelerates the flow entering the impeller and reduces the leading edge separation.

- (5) When $Q = 0.37 \text{ m}^3/\text{s}$

The boundary plane between the main flow and the tip leakage flow arrives at the point further upstream of the impeller and forms a circular backflow area in the piping. The leading edge separation further diminishes.

Figure 14 shows lines that equally divide the flow rate obtained from circumferentially integrating the calculation results (two-dimensional streamline obtained from the three-dimensional flow field). The interval of equally dividing lines increases as the flow velocity in the meridian plane direction decreases or backflows occur. In flow rates smaller than $0.52 \text{ m}^3/\text{s}$, at which the tip leakage flow almost covers the (tip side) blade clearance, the interval of equally dividing lines near the impeller leading edge casing expands into vertical incoming flows.

Figure 15 shows the limiting streamlines on the casing surface. It can be seen that the boundary plane of the tip leakage flow and the main flow reached the impeller upstream plane at $0.49 \text{ m}^3/\text{s}$ and that a circular backflow area exists in the inlet piping at $0.37 \text{ m}^3/\text{s}$.

The position of the boundary plane between the main flow and the tip leakage flow is determined by the balance of the momentum of both. The momentum of the main flow in the axial direction decreases with a reduction in flow rate. On the other hand, the pressure difference that creates a tip leakage flow increases with a rise in the blade loading. Besides, separation at the leading edge of the blade at the tip causes a reduction in the momentum of the main flow. At $Q < 0.49 \text{ m}^3/\text{s}$, the pressure difference that forms tip leakage flows exceeded the main flow's momentum in the axial direction, causing the tip leakage flow to start discharge into the impeller upstream surface. This is the cause of a circular backflow formed in the inlet piping.

It is inferred from the calculation results that inducer stall

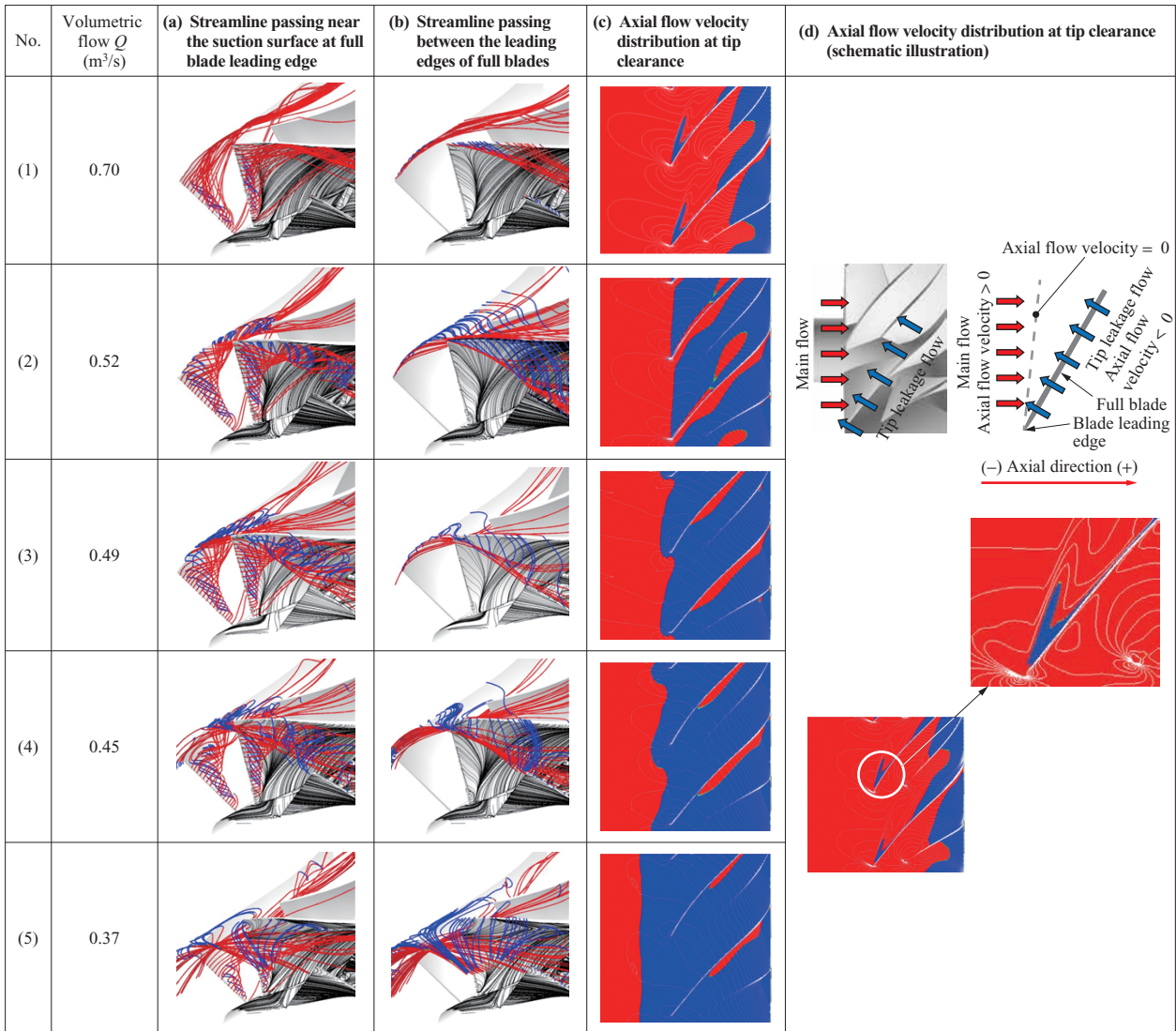


Fig. 13 Streamline passing through near leading edge of full blade suction surface (a), streamline through tip clearance of full blade (b) and axial flow velocity of tip leakage flow (c)

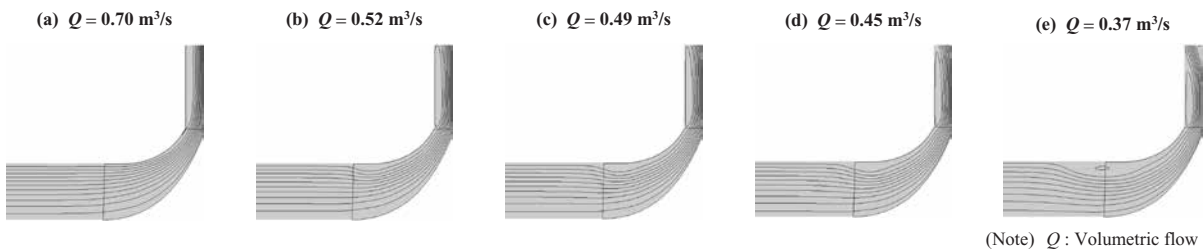


Fig. 14 Circumferentially averaged streamline

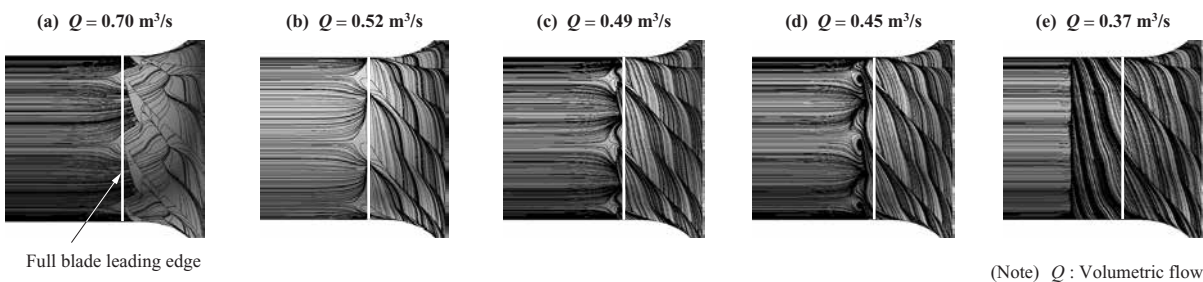


Fig. 15 Limiting streamline on compressor casing

observed in the experiment (see $Q = 0.45 \text{ m}^3/\text{s}$ in **Fig. 6**) was caused by re-entry of the tip leakage flow to the full blade.

4.3.2 Diffuser

Distributions of flow angles and total pressure at II, obtained by calculation, are shown in **Fig. 8**. The figure shows good agreement with measurements until $0.67 \text{ m}^3/\text{s}$. Calculation results for $0.51 \text{ m}^3/\text{s}$ and $0.40 \text{ m}^3/\text{s}$ show a pattern of smaller flow angles on the hub side (leaning towards radial direction) and the presence of a high total pressure area on the hub side, as in the case of $Q \geq 0.67 \text{ m}^3/\text{s}$. On the other hand, the measurement results indicate a tendency where flow angles and total pressure distributions become uniform. This is presumably because the flow distributions become uniform in the span direction as a result of improvement of the flows on the shroud by the blockage due to separation that occurred on the hub side.

Figure 16 shows limiting streamlines at the vaneless diffuser. Flow rates almost match the results of the oil flow visualization method shown in **Fig. 9**. Separation is only observed on the shroud side at (1) $0.67 \text{ m}^3/\text{s}$ of **Fig. 16** as in the case of the oil flow visualization results. The pattern of backflows occurring downstream of the hub side and upstream of the shroud side as observed at (2) $0.52 \text{ m}^3/\text{s}$ in the oil flow visualization results occurs at (3) $0.38 \text{ m}^3/\text{s}$ in CFD. The flow pattern where the areas near both the hub and shroud surfaces are covered by backflows did not occur even at (4) $0.18 \text{ m}^3/\text{s}$. In this calculation method, it is presumed that the discrepancy between the calculation and experiment results increased because the method could not reproduce blockage resulting from separation that occurred at the vaneless diffuser at $Q < 0.52 \text{ m}^3/\text{s}$, where rotating stall occurs.

5. Conclusion

The results of experiments with a compressor composed of a VLD with no inlet pinch were compared with the results of steady calculation with CFD, and the following findings were obtained:

- (1) Measurement and calculation results match each other well with respect to stall or the growth of backflows that occur near the inducer and impeller inlets.
- (2) The calculation results were analyzed, and the condition of flows at the inducer was clarified. It was also found that the tip leakage flow may have reached the leading edge of the full blade at a flow rate that was thought to be a stall point in the experiment.
- (3) It was revealed that unpredictable regions exist with CDF alone. When separated flows steadily exist at the vaneless diffuser, CFD can reproduce the measurement results with relatively high accuracy. On the other hand, it failed to reproduce a flow field obtained by a three-hole yaw-meter and the oil flow visualization method at flow rates smaller than that at which rotating stall was observed. Therefore, the discrepancy between the compressor performance estimated by CFD and the experiment results increased at those flow rates.

In designing a centrifugal compressor, a method that uses









No.	Volumetric flow Q (m^3/s)	(a) Hub side	(b) Shroud side
(1)	0.67		
(2)	0.52		
(3)	0.38		
(4)	0.18		

Fig. 16 Limiting streamline on vaneless diffuser (hub side (a) and shroud side (b))

cyclic symmetric boundary conditions for a single pitch of an impeller and conducts steady calculation is generally used. This paper indicated that the accuracy of CFD (prediction of time-averaged performance) decreases when rotating stall, which is an unsteady phenomenon, occurred in a vaneless diffuser. At this moment, it takes lots of time to conduct unsteady calculation based on full modeling including the entire blades, and it is difficult to apply such time-consuming calculations to design work that requires trial and error in its development process. Therefore, when a centrifugal compressor is designed in which there is a possibility of the vaneless diffuser stalling, it is necessary to use a combination of the experimental formulas for stall, the relevant database and CFD. To realize this, experimental and analytical research on rotation stall phenomena plays an important role.

REFERENCES

- (1) M. V. Casey : Turbomachinery Design Using CFD AGARD Lecture Series 195 (1994. 5) pp. 6-1–6-24
- (2) G. Eisenlohr, P. Dalbert, H. Krain, H. Proell, F-A. Richer and K-H. Rohne : Analysis of the Transonic Flow at the Inlet of a High Pressure Ratio Centrifugal Impeller ASME 98-GT-24 (1998. 6) pp. 1-11

- (3) H. Tamaki : Application of CFD to Compressor Design Turbomachinery Vol. 28 No. 11 (2000. 11) pp. 669-675
- (4) T. Kawakubo : CFD Analysis of Centrifugal and Mixed-Flow Turbomachinery Turbomachinery Vol. 32 No. 5 (2004. 5) pp. 304-313
- (5) H. Tamaki, M. Unno, T. Kawakubo, R. Numakura, and A. Yamagata : Performance Improvement of High-Speed Turbomachinery by CFD Journal of IHI Technologies Vol. 49 No. 2 (2009. 6) pp. 108-117
- (6) S. Oouchida, H. Tamaki, T. Kawakubo, K. Yamada and M. Maruyama : Internal Flow Measurements of Turbomachinery using PIV Journal of IHI Technologies Vol. 53 No. 2 (2013. 6) pp. 59-66
- (7) D. Kato, S. Goto, T. Kato, T. Wakabayashi and H. Ochiai : Development of Simple and High-Performance Technology for Compressors IHI ENGINEERING REVIEW Vol. 41 No. 1 (2008. 2) pp. 13-19
- (8) H. Tamaki, S. Goto, M. Unno and A. Iwakami : The Effect of Clearance Flow of Variable Area Nozzles on Radial Turbine Performance ASME GT2008-50461 (2008. 6) pp. 1 519-1 529
- (9) H. Tamaki, M. Unno, T. Kawakubo and Y. Hirata : Aerodynamic Design to Increase Pressure Ratio of Centrifugal Compressors for Turbochargers ASME GT2009-59160 (2009. 11) pp. 1 171-1 184
- (10) H. Tamaki : Effect of Recirculation Device with Counter Swirl Vane on Performance of High Pressure Ratio Centrifugal Compressor Journal of Turbomachinery Vol. 135 No. 5 (2012. 9) 051036-1-12